Fragmentation of ^{40}Ca, ^{48}Ca, ^{58}Ni and ^{64}Ni at 140 MeV/u

M. Mocko,[1,2,*] M. B. Tsang,[1,2] L. Andronenko,[3,1] M. Andronenko,[3,1]

F. Delaunay,[1] M. Famiano,[1] T. Ginter,[1] V. Henzl,[4,1] D. Henzlová,[4,1] H. Hua,[1]

S. Lukyanov,[1,5] W. G. Lynch,[1,2] A. Rogers,[1,2] M. Steiner,[1] A. Stolz,[1]

O. Tarasov,[1,5] M.-J. van Goethem,[1] G. Verde,[1] M. S. Wallace,[1,2] and A. Zalessov[1]

[1]National Superconducting Cyclotron Laboratory, Michigan

State University, East Lansing, Michigan 48824, USA

[2]Department of Physics & Astronomy, Michigan

State University, East Lansing, Michigan 48824, USA

[3]PNPI, Gatchina, Leningrad district 188300, Russian Federation

[4]Gesellschaft für Schwerionenforschung, D-64291 Darmstadt, Germany

[5]Flerov Laboratory of Nuclear Reactions, Joint Institute for Nuclear

Research, 141980 Dubna, Moscow region Russian Federation

(Dated: September 28, 2006)

Abstract

We have measured fragment cross-sections of projectile fragmentation reactions using primary beams of ^{40}Ca, ^{48}Ca, ^{58}Ni, and ^{64}Ni at 140 MeV/u on ^{9}Be and ^{181}Ta targets. The cross-sections were obtained by integrating the momentum distributions of isotopes with $Z \geq 5$ measured in the A1900 fragment separator. We compare the extracted cross-sections to the predictions of the empirical parameterization of fragmentation cross-sections (EPAX).

---

*Corresponding author: mocko@nscl.msu.edu

1

I.   INTRODUCTION

Projectile fragmentation is a well established technique for the production of rare isotope beams used by many radioactive ion-beam facilities around the world [1, 2, 3]. Even though the first pioneering fragmentation experiments were performed more than 30 years ago in Berkeley [4, 5], we still do not fully understand the reaction mechanism. Some simplifying characteristics have been observed at high incident energies. For example, in peripheral collisions at energies greater than 200 MeV/u, many experimental observables such as charge distributions and multiplicity distributions approach values that vary little with incident energy and target mass [6, 7, 8]. This "limiting fragmentation" behavior forms the basis for the EPAX parameterization [8]. EPAX codes have been used routinely to calculate secondary beam production rates in many radioactive ion beam facilities [1, 2, 9], including expected beam rates for next generation rare isotope accelerators [10, 11, 12]. EPAX parameterization is not based on a specific theory, rather, its parameters have been derived from fits to several data sets of production cross-sections measured under a wide variety of experimental conditions. The original EPAX parameterization included only target spallation data [7]. It was revisited in 2000 and improved by including projectile fragmentation data available at that time [8]. These data sets lack fragment cross-sections measured at intermediate energies. Such data will put some constraints on the threshold energy of "limiting fragmentation" and further improve EPAX parameterization for intermediate energy facilities.

In this paper, we present comprehensive fragment cross-section measurements of projectile fragmentation of ^{40}Ca, ^{48}Ca, ^{58}Ni, and ^{64}Ni beams on two targets, ^{9}Be and ^{181}Ta at 140 MeV/u. This paper mainly focuses on the experimental measurements of these cross-sections and the comparison of the measured cross-sections to EPAX predictions. We will address the physics of projectile fragmentation, including the dependence on projectile and target asymmetry and comparisons of our data to fragmentation models in a future paper.

II.   EXPERIMENTAL SETUP

The fragmentation experiments were carried out using the Coupled Cyclotron Facility (CCF) [9] at the National Superconducting Cyclotron Laboratory (NSCL) at Michigan State University (MSU). Primary beams of ^{40}Ca, ^{48}Ca, ^{58}Ni, and ^{64}Ni isotopes with an incident

energy of 140 MeV/u were produced by the K500⊗K1200 coupled cyclotrons. We used two reaction targets: 100 mg/cm^2 ^{9}Be and 220 mg/cm^2 ^{181}Ta foils. The target thicknesses were chosen such that the energy losses of the primary beams in the targets are similar. Data could then be taken with both targets using the same magnetic settings, thus, minimizing the number of magnetic rigidity settings required in the experiments. The emitted fragments were collected and identified using the A1900 fragment separator [13, 14, 15]. Fig. 1 shows the A1900 fragment separator as a part of the CCF facility. It consists of four supercon-ducting dipoles, each with a radius of 3 m and a bending angle of 45°. In addition, it uses 24 quadrupole magnets housed in 8 cryostats. The A1900 fragment separator was designed with a large angular acceptance of 8 msr. Other fundamental parameters such as resolving power (2915), momentum dispersion (59.5 mm/%) and maximum magnetic rigidity (6 Tm) [14] were designed to match the beam properties of the CCF. A detailed description of the A1900 can be found in Ref. [13, 14, 15].

All the measurements were performed using the A1900 fragment separator in a narrow momentum acceptance mode. The momentum opening, dp/p, was limited to 0.2% using a slit in the dispersive image of the spectrometer (labeled as I2 in Fig. 1). In this configuration the measured particles have trajectories close to the axis of the fragment separator simpli-fying the transmission calculation. Furthermore, a narrow momentum acceptance allows measurements of fragment cross-sections in the magnetic rigidity region between primary beam charge states. The disadvantage is that in order to measure momentum distributions over a wide range of fragmentation products, we had to take measurements over many mag-netic settings. For ^{40}Ca we took measurements between 3.2–4.2 Tm in 33 steps, and for ^{48}Ca we scanned the region between 3.2–5.1 Tm in 50 settings. For ^{58}Ni and ^{64}Ni beams, we took data between 3.25–4.3 Tm in 26 steps, and 3.3–4.5 Tm in 34 settings, respectively. To avoid excessive dead-time in the data acquisition and to avoid efficiency problems with the energy loss detector (PIN) at the focal plane, the primary beam intensity was optimized at each magnetic rigidity such that the counting rate of PIN detector was approximately 700–900 counts per second.

All fragments produced in our study were fully stripped of electrons. Hence they could be identified using the $B\rho$-ToF-ΔE method [1], on an event-by-event basis. The magnetic rigidity, $B\rho$, was determined from the magnetic setting of the A1900 fragment separator. The time of flight, ToF, was measured with the plastic scintillator (SCIN) timed with
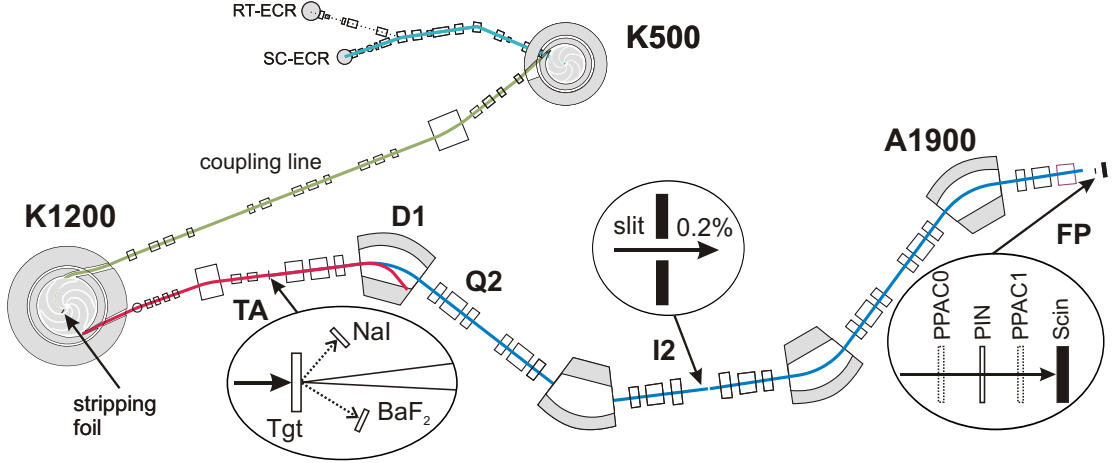
3

FIG. 1: (Color online) The A1900 fragment separator in stand-alone mode. Beam intensity monitors (NaI(Tl) and BaF_2) were located at the target station (TA). The momentum slit at the intermediate image (I2) defined the momentum opening (0.2% in dp/p). The detector setup at the focal plane (FP) was used to identify fragments. The first dipole (out of four) is labeled D1 and the second quadrupole triplet (out of eight) is labeled as Q2.

respect to the Radio Frequency (RF) of the coupled cyclotrons. The energy loss, ΔE, was measured with a 470 μm thick silicon Positive Intrinsic Negative (PIN) detector. Both SCIN and PIN are part of the A1900 Focal Plane detection system as shown inside the right oval in Fig. 1. During the experiment, position sensitive Parallel Plate Avalanche Counters (PPAC0 & PPAC1) placed before and after the PIN detector monitored that fragments hit the sensitive area of the PIN detector. The coincidence requirement is removed in the data analysis to avoid correction for the efficiencies of the PPACs which vary with elemental charge.
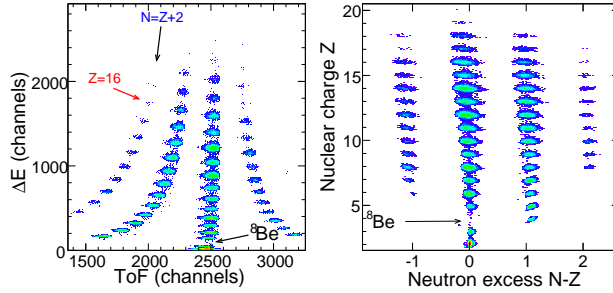
FIG. 2: (Color online) Raw (left panel) and calibrated (right panel) particle identification spectrum for ^{48}Ca+^{9}Be reactions at $B\rho = 3.2$ Tm.

A typical raw experimental particle identification pattern is shown in the left panel of Fig. 2. The example provided is for the ^{48}Ca+^{9}Be reaction at $B\rho = 3.2$ Tm. We can see a clear separation of individual groups of events. The nearly vertical line located near ToF channel 2500 is the line of fragments with $N = Z$. The time of flight spectrum was set up such that the neutron-rich fragments are located to the left and the neutron-deficient fragments are located to the right of this line. Thus the leftmost band corresponds to the $N = Z + 2$ line. By recognizing the typical features of the PID spectrum and locating the hole corresponding to particle unbound ^{8}Be nucleus, we can identify all nuclides. From the detector calibrations, we can generate a calibrated PID spectra of the fragment charge number Z vs. the neutron excess, $N - Z$, as shown in the right panel of Fig. 2. All fragments are clearly separated in all our experiments.

Each experimental run took data for one $B\rho$ setting. The number of events, $N(A, Z)$, for a fragment with mass number, A, and proton number, Z, was extracted from the calibrated PID spectra. The differential cross-sections, $d\sigma/dp$, were calculated taking into account the number of beam particles, N_B, number of target nuclei per square centimeter, N_T, live-time ratio, τ_{LIVE}, and the transmission efficiency through the A1900 fragment separator, ε,

$$\frac{d\sigma}{dp}(A, Z) = \frac{N(A, Z)}{N_T N_B \Delta p \tau_{LIVE}} \cdot \frac{1}{\varepsilon}, \tag{1}$$

where Δp denotes the momentum opening.

The transmission efficiency correction, ε, is assumed to be factorized into two independent components: momentum corrections and angular corrections. Momentum corrections take into account the loss of fragments with momentum not centered at the momentum slit. These fragments travel in trajectories that deviate from the central trajectory and sometimes may
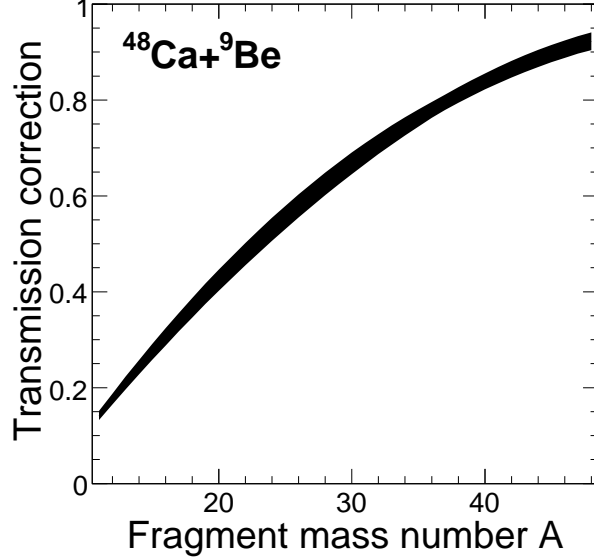
FIG. 3: Dependence of the transmission correction, ε, on the fragment mass number, A, for $^{48}\text{Ca}+^{9}\text{Be}$ reactions.

not be transmitted to the focal plane. The effect is independent of fragment species and the $B\rho$ setting. A correction value of $96 \pm 2\%$ is obtained from simulations using the universal Monte Carlo charged-ion transport code MOCADI [16]. The angular correction accounts for finite angular acceptance of the A1900 fragment separator in the perpendicular (transverse) plane with respect to the beam direction. The current experiment does not measure the momentum in the transverse direction. Based on Ref. [17], the perpendicular momentum distribution for a fragment with mass number, A_F, is modeled by a Gaussian function with variance, $\sigma_\perp$, prescribed as [17]:

$$\sigma_\perp^2 = \sigma_0^2 \frac{A_F(A_P - A_F)}{A_P - 1} + \sigma_D^2 \frac{A_F(A_F - 1)}{A_P(A_P - 1)}, \tag{2}$$

where A_P is the mass number of the projectile and σ_D is the orbital dispersion. The first term in Eq. (2) comes from the Goldhaber model [18], which describes the width of longitudinal momentum distribution of fragments produced at relativistic projectile energies. The value σ_0 is determined by fitting the experimental longitudinal momentum distributions. Values of 106 ± 4 (101 ± 5) MeV/c and 109 ± 5 (106 ± 4) MeV/c were obtained for the $^{40}\text{Ca}+^{9}\text{Be}$ (^{181}Ta) and $^{48}\text{Ca}+^{9}\text{Be}$ (^{181}Ta) systems, respectively. Similarly, values of 113 ± 3 (110 ± 3) MeV/c and 117 ± 5 (114 ± 3) MeV/c were obtained for the $^{58}\text{Ni}+^{9}\text{Be}$ (^{181}Ta) and $^{64}\text{Ni}+^{9}\text{Be}$ (^{181}Ta) systems, respectively. The second term in Eq. (2) takes into account the deflection of the

projectile by the target nucleus [19], and is significant only at low and intermediate energies. We estimated the orbital dispersion parameter, σ_D, to be 185 ± 15 MeV/c for all systems, based on the ^{16}O fragmentation data measured at 117 MeV/u [17]. The parameterization in Eq. (2) has been confirmed recently by the fragment transverse momentum distributions measured at the NSCL with the S800 spectrograph for the ^{64}Ni+^{9}Be reaction [20]. Portions of the Gaussian angular distributions transmitted through the A1900 fragment separator define the angular transmission, and were calculated using LISE++ [21] and verified with MOCADI simulations. The final transmission correction, ε, consisting of the product of the angular and momentum corrections, is plotted in Fig. 3 for the ^{48}Ca+^{9}Be reactions. Similar plots are obtained for all eight reactions studied. ε varies from 0.96 for the fragments close to the projectile to approximately 0.3 for the lightest fragments in our analysis.

In our fragmentation measurements the primary beam intensity varied between 10^6 pps to 10^{10} pps. Two detector systems were required to accommodate the large dynamic range of primary beam intensity. The first detector configuration was an array of four NaI(Tl) crystals designed to detect light charged particles emitted in the reaction at low beam intensity ($< 10^9$ pps). The NaI(Tl) array consisted of 4 crystals mounted on a ladder approximately 30 cm from the target right outside the target chamber at an angle of approximately 45° with respect to the beam direction. The second beam intensity monitor was a single BaF$_2$ crystal designed to detect gamma rays emitted in the reaction at high beam intensity ($> 10^9$ pps). The BaF$_2$ detector shielded by a lead fortress, was placed outside the target chamber on the floor, approximately 130 cm from the target at an angle of approximately 72° with respect to the beam direction. The general location of these two systems is shown by the schematic in the oval labeled as TA in Fig. 1. Both primary beam intensity monitors were calibrated using a Faraday cup positioned approximately 10 cm in front of the production target. (For the ^{58}Ni beam measurement, this Faraday cup was not available. Instead, we used a Faraday cup located right outside the K1200 cyclotron.) Since the count rate of the beam monitors depends on nuclear reactions, calibration is obtained for each beam and target combination. The uncertainty of the beam intensity calibration was determined to be 7–8% [22].
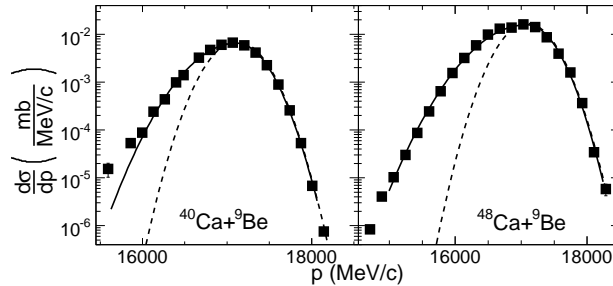
FIG. 4: Momentum distributions for ^{33}P produced in fragmentation of ^{40}Ca (left panel) and ^{48}Ca (right panel) primary beams. The solid curve represents a fit with Eq. (3) and the dotted curve is a Gaussian fit to the right side of the momentum distribution to show the asymmetry of the experimental distributions.

III. MOMENTUM DISTRIBUTIONS

The momentum distributions were obtained by plotting individual differential cross-sections as a function of momentum (calculated from the magnetic rigidity). Contrary to the symmetric Gaussian distributions observed in relativistic heavy-ion fragmentation, the momentum distributions obtained from projectile fragmentations at intermediate energy are asymmetric [19, 23, 24] and cannot be represented by a single Gaussian function. Fig. 4 shows typical parallel momentum distributions of ^{33}P from ^{40}Ca+^{9}Be (left panel) and ^{48}Ca+^{9}Be (right panel) reactions. The dashed lines represent fits with a single Gaussian function. As the distributions have low momentum tails, we fit the data with the following function [24]:

$$\frac{\mathrm{d}\sigma}{\mathrm{d}p} = \begin{cases} S \cdot \exp\left(-(p - p_0)^2/(2\sigma_L^2)\right) & \text{for } p \leq p_0, \\ S \cdot \exp\left(-(p - p_0)^2/(2\sigma_R^2)\right) & \text{for } p > p_0, \end{cases} \quad , \tag{3}$$

where S is the normalization factor, p_0 is the peak position of the distribution, σ_L and σ_R are widths of "left" and "right" halves of two Gaussian distributions used to fit the momentum distributions. The solid curves in Fig. 4 show the best fits obtained by minimization of χ^2 using Eq. (3). For most fragments we observe very good agreement between data and fit over three orders of magnitude.

8

IV. CROSS-SECTION MEASUREMENTS

The cross-section of a fragment was determined by integrating the area of its momentum distribution. For fragments with well-measured momentum distributions such as those shown in Fig. 4, the cross-sections were extracted from fitting the momentum distributions using Eq. (3). However, approximately 20–30% of the measured fragments had incomplete momentum distributions that may consist of only a few points near the top of the peak. For these fragments, we used the systematics of p_0, σ_L, and σ_R obtained from fragments with complete momentum distributions to calculate the cross-sections with Eq. (3).

Uncertainties in the final fragmentation cross-sections were calculated based on the statistical uncertainty, beam intensity calibration (7–8%), errors from the fitting procedure and transmission uncertainty (2–8%). For fragments measured with incomplete momentum distributions, additional systematic errors stemming from the extrapolation of the parameters of p_0, σ_L, and σ_R were included. The overall uncertainties of the fragmentation cross-sections are 7–12%.

An overall view of the fragment cross-sections in the style of the nuclear chart is shown in Fig. 5. The range of the measured cross-sections span over 8 orders of magnitude, from nb to hundreds of mb. ^{50}Ca produced in the reaction of ^{58}Ni+^{9}Be had the lowest cross-section measured in the present work. To achieve the measurement of such low cross-section (0.41 ± 0.16 nb), we used a thick ^{9}Be target (578 mg/cm^2). In addition, an Al wedge (240 mg/cm^2) was placed at the dispersive Image 2 position to further separate the fragments with the same A/Q ratios. The wedge is especially effective in deflecting the light charged fragments from reaching the focal plane detector, thus reducing the counting rate of the PIN detector. The measured isotope cross-sections for the ^{40}Ca+^{9}Be (top) and ^{48}Ca+^{9}Be (bottom) reactions are presented in the left panel of Fig. 5. For reference, the projectile is represented by the symbol of a box with a cross inside and stable isotopes are highlighted with the black framed boxes. The number of nuclei measured in ^{48}Ca fragmentation (202) is nearly twice that measured in ^{40}Ca (111). As expected, many more neutron-rich fragments are produced by the neutron-rich projectile ^{48}Ca. The cross-sections of 196 and 243 isotopes from the fragmentation of ^{58}Ni and ^{64}Ni beams, respectively are presented similarly in the right panel of Fig. 5. In general, for all four projectiles, the fragment production landscapes look similar for both the ^{9}Be and ^{181}Ta targets.
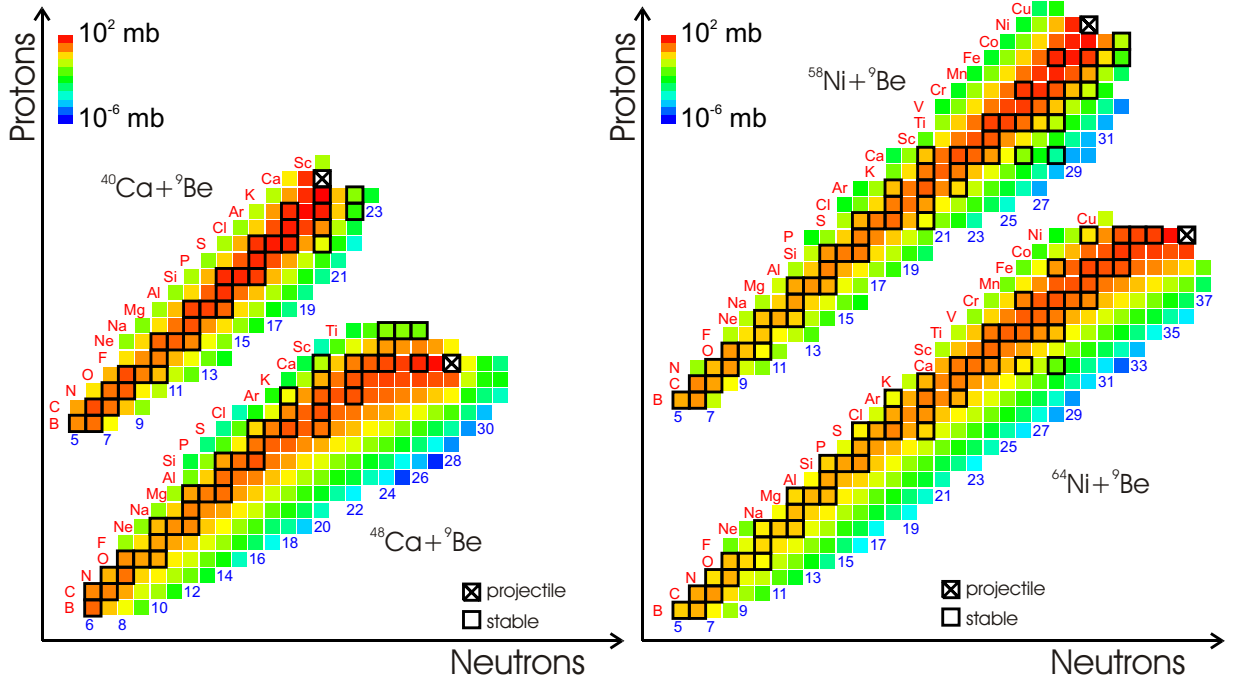
FIG. 5: (Color online) Isotope cross-sections measured in the fragmentation of ^{40,48}Ca projectiles on ^{9}Be target (left panel) and in the fragmentation of ^{58,64}Ni projectile on ^{9}Be target (right panel).

A. Comparison to EPAX

For quantitative comparisons with EPAX, the experimentally determined fragmentation production cross-sections for the eight reaction systems are plotted in Fig. 6 (^{40}Ca+^{9}Be), Fig. 7 (^{40}Ca+^{181}Ta), Fig. 8 (^{48}Ca+^{9}Be), Fig. 9 (^{48}Ca+^{181}Ta), Fig. 10 (^{58}Ni+^{9}Be), Fig. 11 (^{40}Ca+^{181}Ta), Fig. 12 (^{64}Ni+^{9}Be), and Fig. 13 (^{64}Ni+^{181}Ta). Each panel represents isotope cross-section data for one element, plotted as a function of neutron excess, $N - Z$, of each isotope. Filled squares represent fragmentation data from the present work. The nucleon pick-up and exchange cross-sections are shown as filled triangles. All cross-sections shown as solid curves in Fig. 6–13 were computed with the new improved EPAX formula [8]. EPAX does not calculate pick-up cross-sections and the description of the light fragments (with $A < 0.5 A_P$) are generally not as good as the predictions for fragments near the

projectiles because light fragments may be produced in more central collisions from other reaction mechanism such as multifragmentation. The maxima of very light elements $Z < 9$, which may be produced in more central collisions, do not agree with EPAX predictions. In general, isotope distributions from EPAX are wider than the measured ones, resulting in over-predictions of the fragments for the very neutron-rich and proton-rich isotopes.

For secondary beam rate estimates, it is more important to identify the isotopes whose cross-sections are over-predicted by EPAX. In Fig. 14, we plot the ratios of the measured cross-sections to EPAX predicted cross-sections in the nuclear chart format for the Ca and Ni projectile fragmentation in a similar convention as in Fig. 5. Ratios with values larger than 1 are shown in light grey. This group includes most of the cross-sections of stable fragments and fragments near the projectile. For the neutron-rich projectile ^{48}Ca, neutron-rich N, O and F isotopes are also produced in abundance. Similarly, for the ^{64}Ni projectile, we see ratios greater than 1 for the production of neutron-rich Ne to K isotopes. Ratios with values less than 1 are classified in three different groups. EPAX severely over-estimates production of fragments mainly in the regions of extremely neutron-rich and proton-rich nuclei. These nuclei at the edge of our plots are at the limit of our current cross-section measurement sensitivity. Thus it is reasonable to assume that the disagreement with EPAX will get worse for more exotic nuclei.

B. Comparison to other data

In addition to our data, Fig. 6 also shows fragmentation data of ^{40}Ca on a hydrogen target at 356 MeV/u [25]. The latter data are shown as open squares. Compared to our data, the isotope distributions obtained from the hydrogen target tend to be narrower than our data and the cross-sections are smaller. The narrower isotopic distributions generally indicate lower excitation energy reflecting lower center of mass energy for the system with hydrogen target.

Fragment cross-sections measured in the reaction ^{48}Ca+^{9}Be are compared to the fragmentation data measured at 212 MeV/u [26] shown as open squares in Fig. 8. Even though the fragmentation data of Ref. [26] were included in extracting the EPAX parameters, the deviation of this data set from the overall EPAX fit was noted in the original paper [8]. On the other hand, our fragmentation data seem to agree pretty well with EPAX predictions

except for a small shift of the maximum for elements (S–Ca) close to the projectile.

More recently, cross-sections of ^{46,47}Ca, ^{44,45,46,47}K, ^{41,42,44,45}Ar, and ^{39,40,41,42}Cl isotopes have been measured in the projectile fragmentation of ^{48}Ca+^{2}H at 104 MeV/u [27] with the S800 spectrometer at NSCL. These measured data are plotted in Fig. 8 as open triangles. As noted in Ref. [28], the cross-sections for fragments with few nucleons removed obtained with the ^{2}H target are not lower than the cross-sections with ^{9}Be target as expected from EPAX. For the Ca and K isotopes, the cross-sections are even higher.

Fragment cross-sections measured in the reaction ^{58}Ni+^{9}Be are compared to the data at 650 MeV/u [28] measured at GSI shown as open squares in Fig. 10. The latter experiment focused on the production of proton-rich fragments with $21 \leq Z \leq 28$. Where there are overlapping data points, an interesting trend is observed. The fragment cross-sections from the GSI experiment are consistently higher by 70% than our data for the proton-rich ($Z > N$) isotopes. In the slightly neutron-rich the GSI data are slightly lower by 30%. Unfortunately there are not enough overlaps between the two sets of data to determine if the widths of the distributions are wider or narrower.

V. SUMMARY

Fragmentation production cross-sections have been measured for ^{40}Ca, ^{48}Ca, ^{58}Ni, and ^{64}Ni primary beams on ^{9}Be and ^{181}Ta targets. More fragments are produced with neutron-rich target. The number of fragments detected in the projectile fragmentation of ^{48}Ca is nearly twice as many as those detected in the projectile fragmentation of ^{40}Ca. At an incident energy of 140 MeV/u, the cross-section distributions predicted by EPAX are wider than the experimental distributions, resulting in over-predictions of cross-sections for very neutron-rich and very proton-rich isotopes. The measured cross-sections should allow improvements of the next version of EPAX parameters which will be applicable for intermediate energy fragmentation reactions.

[1] H. Geissel, P. Armbruster, K. H. Behr, A. Brünle, K. Burkard, M. Chen, H. Folger, B. Franczak, H. Keller, O. Klepper, et al., Nucl. Instrum. Methods Phys. Res., Sect. B **70**, 286 (1992).

[2] T. Kubo, M. Ishihara, N. Inabe, H. Kumagai, I. Tanihata, and K. Yoshida, Nucl. Instrum. Methods Phys. Res., Sect. B **70**, 309 (1992).

[3] B. M. Sherrill, Prog. Theor. Phys. **146**, 60 (2002).

[4] H. H. Heckman, D. E. Greiner, P. J. Lindstrom, and F. S. Bieser, Science **174**, 1130 (1971).

[5] H. A. Grunder, W. D. Hartsough, and E. J. Lofgren, Science **174**, 1128 (1971).

[6] G. Rudstam, Z. Naturforsch., A: Phys. Sci. **21**, 1027 (1966).

[7] K. Sümmerer, W. Brüchle, D. J. Morrissey, M. Schädel, B. Szweryn, and Y. Weifan, Phys. Rev. C **42**, 2546 (1990).

[8] K. Sümmerer and B. Blank, Phys. Rev. C **61**, 034607 (2000).

[9] MSUCL-939 (1994), The K500 ⊗ K1200, A Coupled Cyclotron Facility at the National Superconducting Cyclotron Laboratory.

[10] B. M. Sherrill, Nucl. Instrum. Methods Phys. Res., Sect. B **204**, 765 (2003).

[11] GSI (2006), An International Accelerator Facility for Beams of Ions and Antiprotons, URL `http://www.gsi.de/GSI-Future/cdr/`.

[12] T. Motobayashi, Nucl. Instrum. Methods Phys. Res., Sect. B **204**, 736 (2003).

[13] I. Wiedenhöver, M. Steiner, D. J. Morrissey, B. M. Sherrill, D. Bazin, J. Stetson, A. Stolz, O. Tarasov, J. Yurkon, and the NSCL staff, AIP Conference Proceedings **610**, 937 (2002).

[14] D. J. Morrissey, B. M. Sherrill, M. Steiner, A. Stolz, and I. Wiedenhoever, Nucl. Instrum. Methods Phys. Res., Sect. B **204**, 90 (2003).

[15] A. Stolz, T. Baumann, T. N. Ginter, D. J. Morrissey, M. Portillo, B. M. Sherrill, M. Steiner, and J. W. Stetson, Nucl. Instrum. Methods Phys. Res., Sect. B **241**, 858 (2005).

[16] N. Iwasa, H. Geissel, G. Münzenberg, C. Scheidenberger, T. Schwab, and H. Wollnik, Nucl. Instrum. Methods Phys. Res., Sect. B **126**, 284 (1997).

[17] K. V. Bibber, D. L. Hendrie, D. K. Scott, H. H. Weiman, L. S. Schroeder, J. V. Geaga, S. A. Cessin, R. Treuhaft, Y. J. Grossiord, J. O. Rasmussen, et al., Phys. Rev. Lett. **43**, 840 (1979).

[18] A. S. Goldhaber, Phys. Lett. B **53**, 306 (1974).

[19] R. Dayras, A. Pagano, J. Barrette, B. Berthier, D. M. D. C. Rizzo, E. Chavez, O. Cisse, R. Legrain, M. C. Mermaz, E. C. Pollacco, et al., Nucl. Phys. A **460**, 299 (1986).

[20] S. Lukyanov, private communications.

[21] D. Bazin, O. Tarasov, M. Lewitowicz, and O. Sorlin, Nucl. Instrum. Methods Phys. Res., Sect. A **482**, 307 (2002), URL `http://www.nscl.msu.edu/lise`.

[22] M. Mocko, Ph.D. thesis, Michigan State University (2006).

[23] D. Bazin, D. Guerreau, R. Anne, D. Guillemaud-Mueller, A. C. Mueller, and M. G. Saint-Laurent, Nucl. Phys. A **515**, 349 (1990).

[24] M. Notani, Ph.D. thesis, University of Tokyo (2000).

[25] C.-X. Chen, S. Albergo, Z. Caccia, S. Costa, H. J. Crawford, M. Cronqvist, J. Engelage, L. Greiner, T. G. Guzik, A. Insolia, et al., Phys. Rev. C **56**, 1536 (1997).

[26] G. D. Westfall, T. J. M. Symons, D. E. Greiner, H. H. Heckman, P. J. Lindstrom, J. Mahoney, A. C. Shotter, D. K. Scott, H. J. Crawford, C. McParland, et al., Phys. Rev. Lett. **43**, 1859 (1979).

[27] B. T. Roeder, K. W. Kemper, N. Aoi, D. Bazin, M. Bowen, C. M. Campbell, J. M. Cook, D.-C. Dinca, A. Gade, T. Glasmacher, et al., Phys. Rev. C **74**, 034602 (2006).

[28] B. Blank, S. Andriamonje, R. D. Moral, J. P. Dufour, A. Fleury, T. Josso, M. S. Pravikoff, S. Czajkowski, Z. Janas, A. Piechaczek, et al., Phys. Rev. C **50**, 2398 (1994).
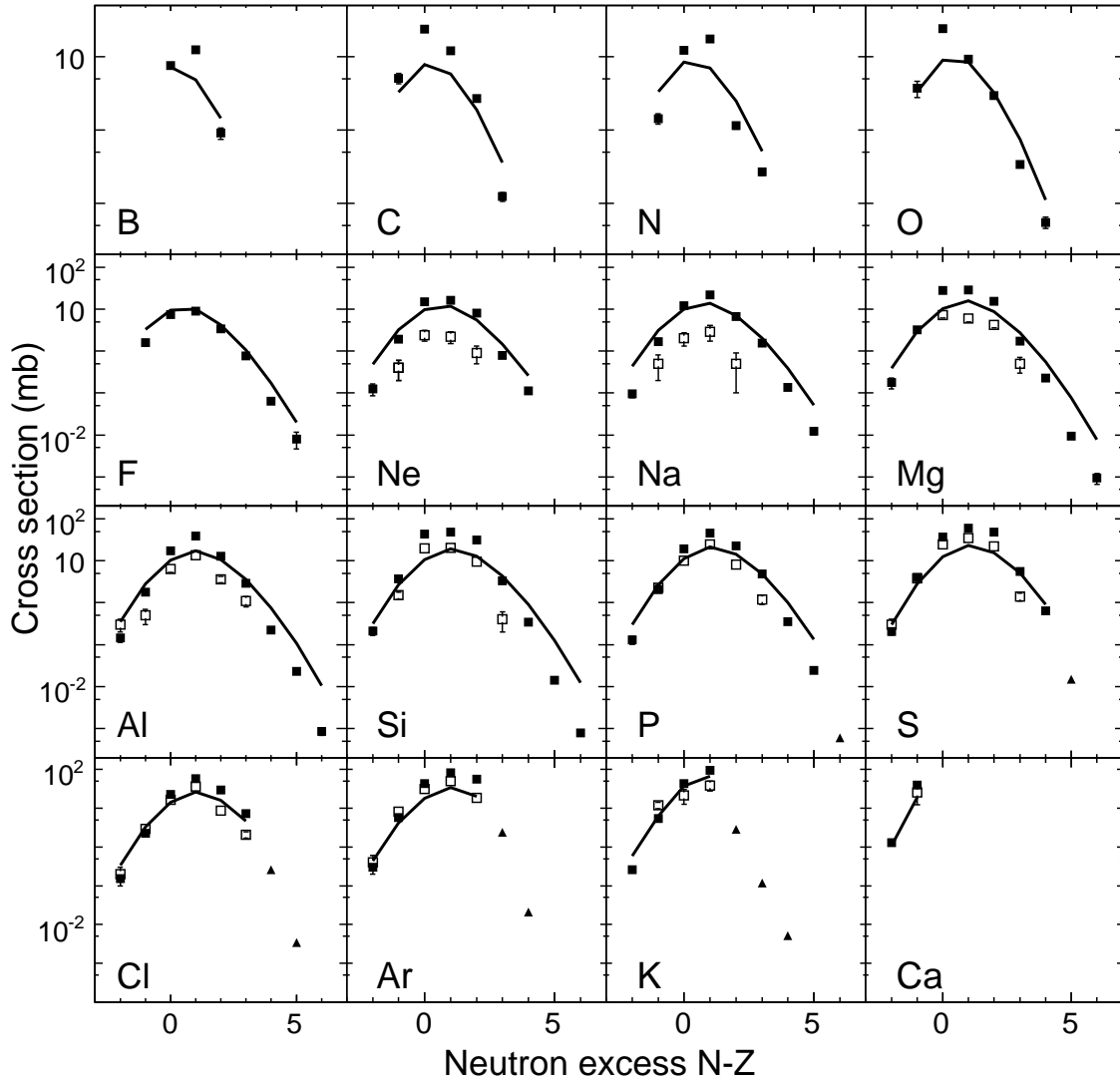
FIG. 6: Measured cross-sections presented as isotope distributions for $5 \leq Z \leq 20$ elements detected in ^{40}Ca+^{9}Be reactions at 140 MeV/u. Experimental fragmentation data are shown as filled squares. Filled triangles show the cross-sections of nucleon pick-up reactions. EPAX predictions are shown as solid lines. Open squares show ^{40}Ca+^{1}H at 356 MeV/u.
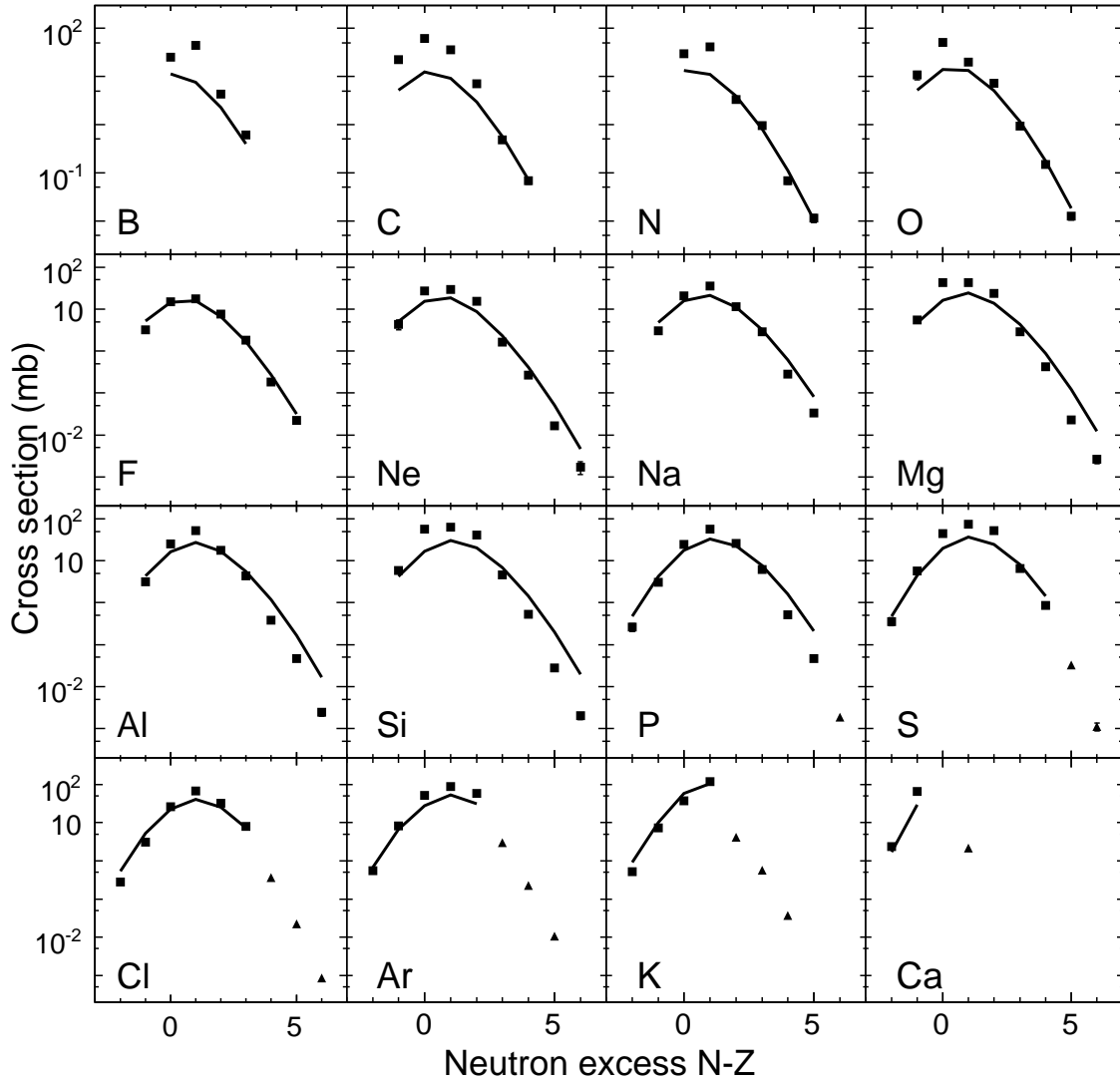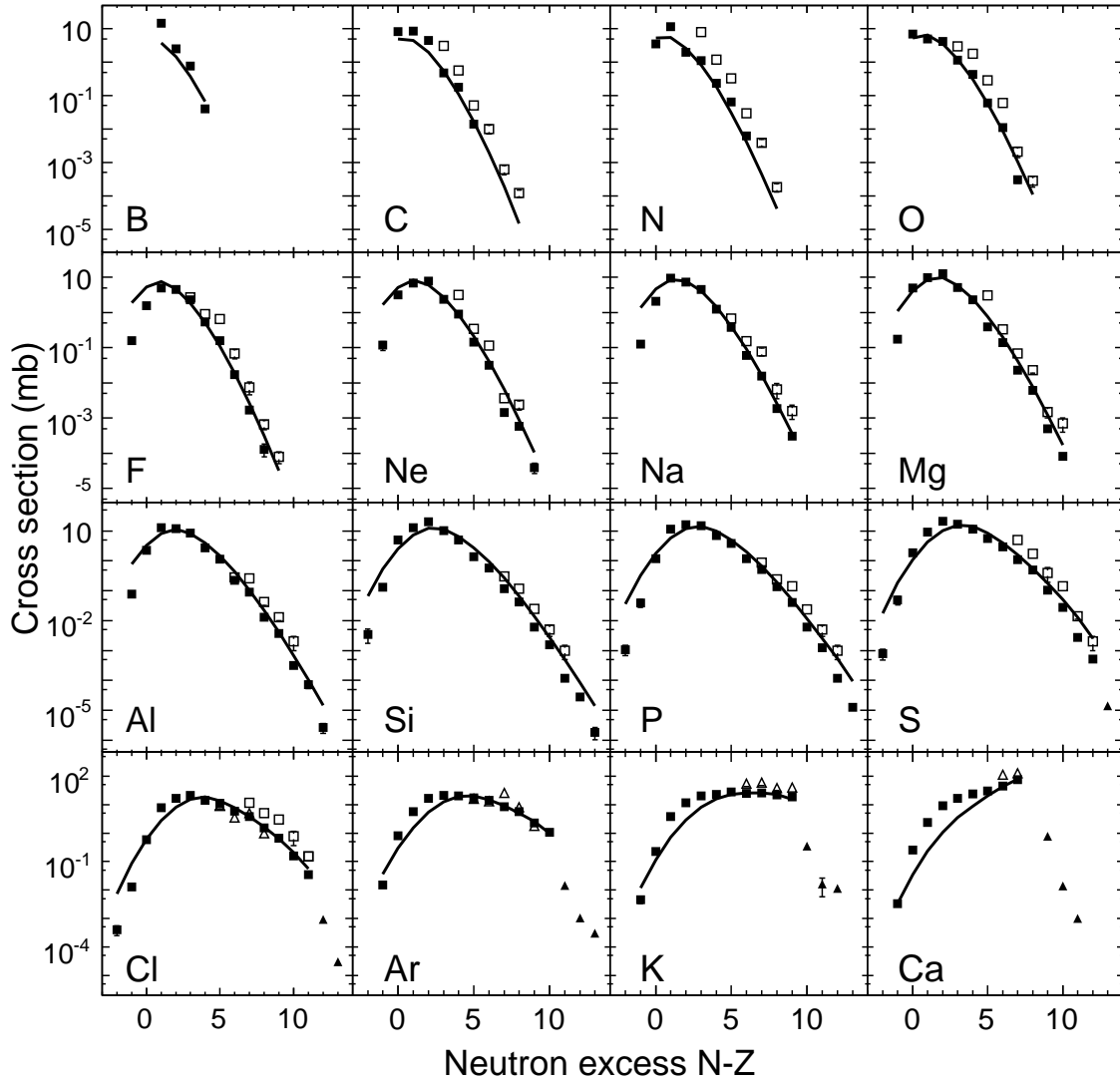
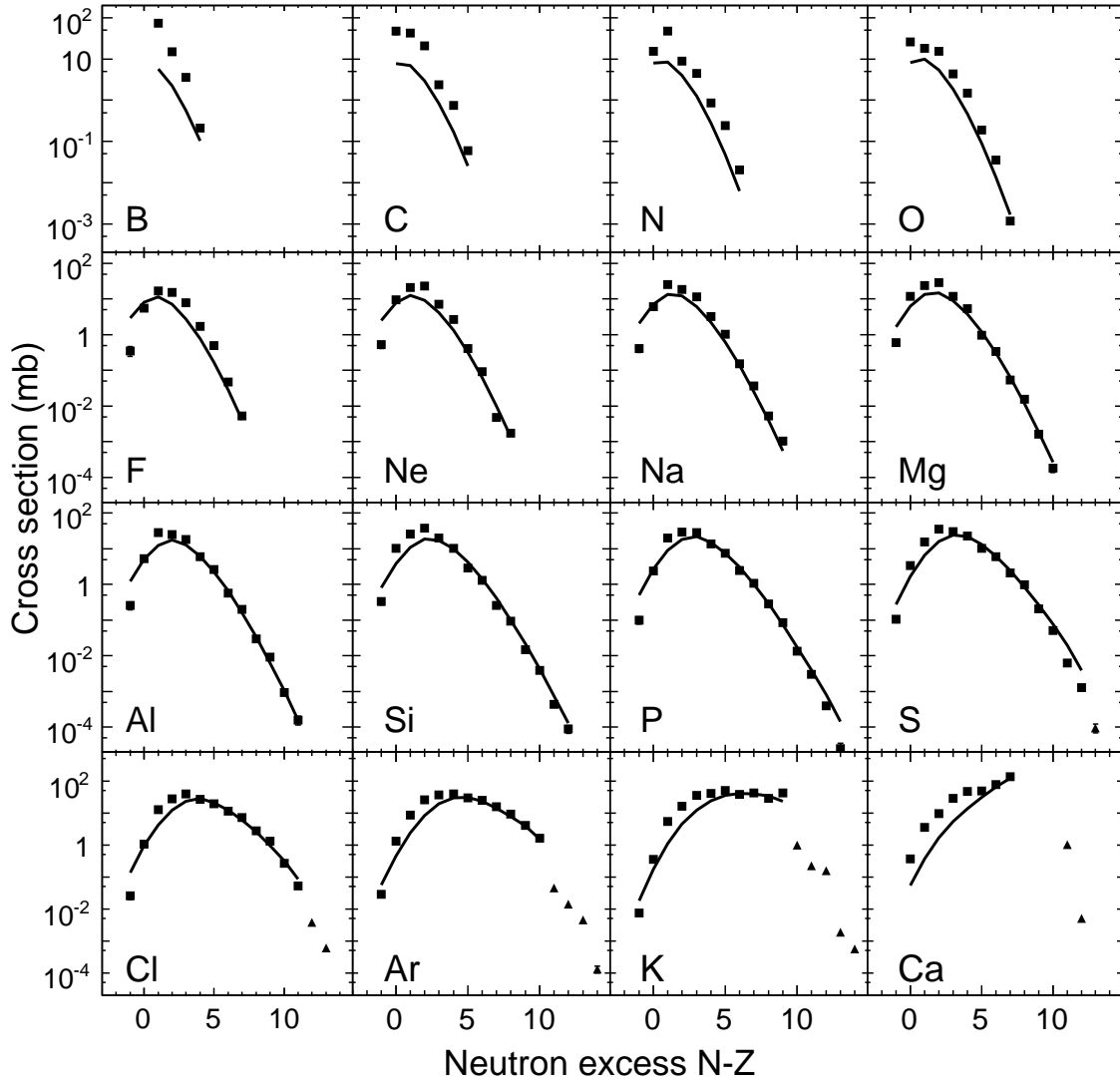FIG. 7: Measured cross-sections presented as isotope distributions for $5 \leq Z \leq 20$ elements detected in ^{40}Ca+^{181}Ta reactions at 140 MeV/u. Experimental fragmentation data are shown as filled squares. Filled triangles show the cross-sections of nucleon pick-up reactions. EPAX predictions are shown as solid lines.

16

FIG. 8: Measured cross-sections presented as isotope distributions for $5 \leq Z \leq 20$ elements detected in ^{48}Ca+^{9}Be reactions at 140 MeV/u. Experimental fragmentation data are shown as filled squares. Filled triangles show the cross-sections of nucleon pick-up reactions. EPAX predictions are shown as solid lines. Open squares show ^{48}Ca+^{9}Be at 212 MeV/u [26]. Open triangles show fragments created in the ^{48}Ca+^{2}H at 104 MeV/u [27].

17

FIG. 9: Measured cross-sections presented as isotope distributions for $5 \leq Z \leq 20$ elements detected in $^{48}Ca+^{181}Ta$ reactions at 140 MeV/u. Experimental fragmentation data are shown as filled squares. Filled triangles show the cross-sections of nucleon pick-up reactions. EPAX predictions are shown as solid lines.
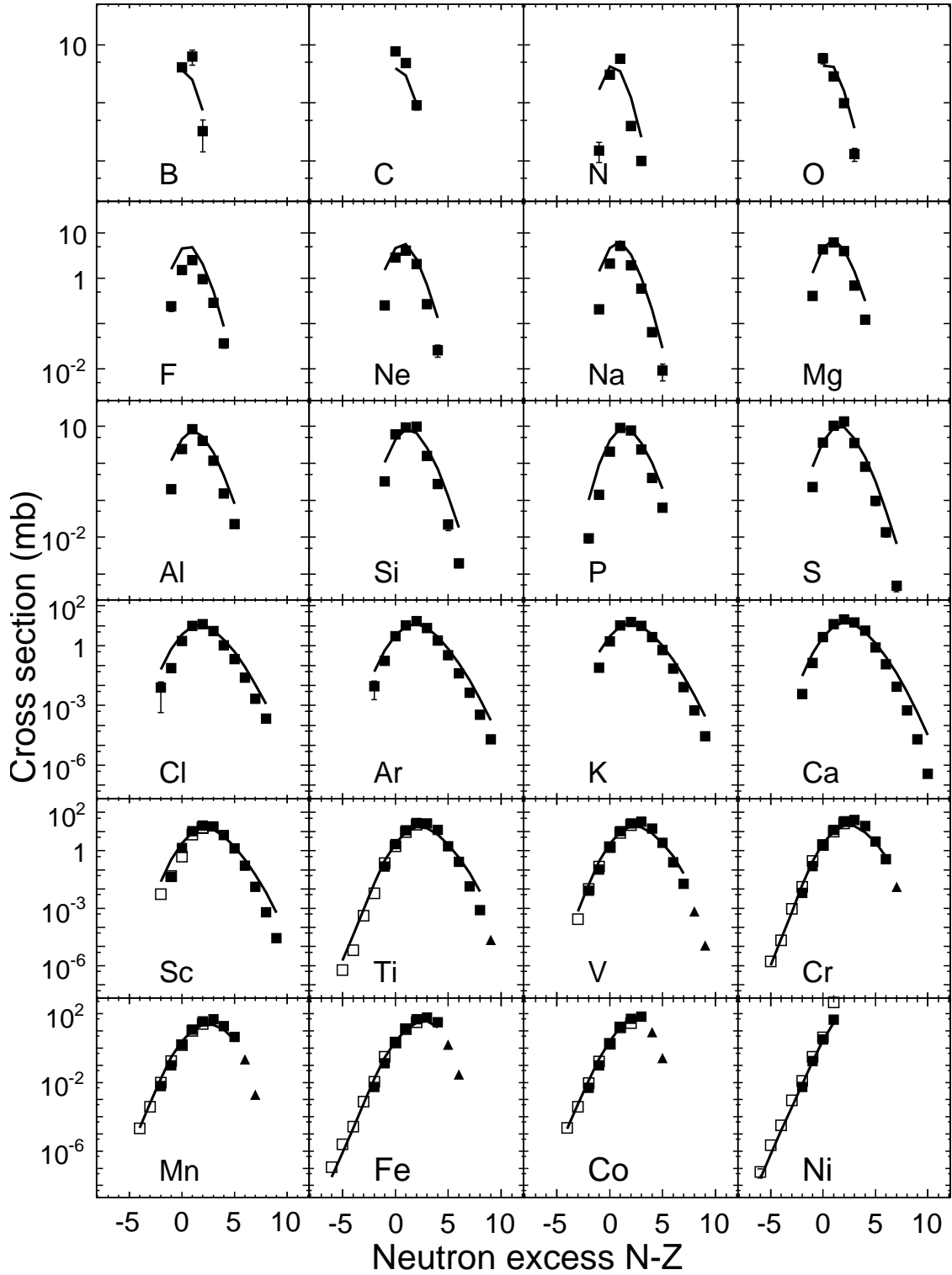
FIG. 10: Measured cross-sections presented as isotope distributions for $5 \leq Z \leq 28$ elements detected in ^{58}Ni+^{9}Be reactions at 140 MeV/u. Experimental fragmentation data are shown as filled squares. Filled triangles show the cross-sections of nucleon pick-up reactions. EPAX predictions are shown as solid lines. Open squares show ^{58}Ni+^{9}Be at 650 MeV/u [28].
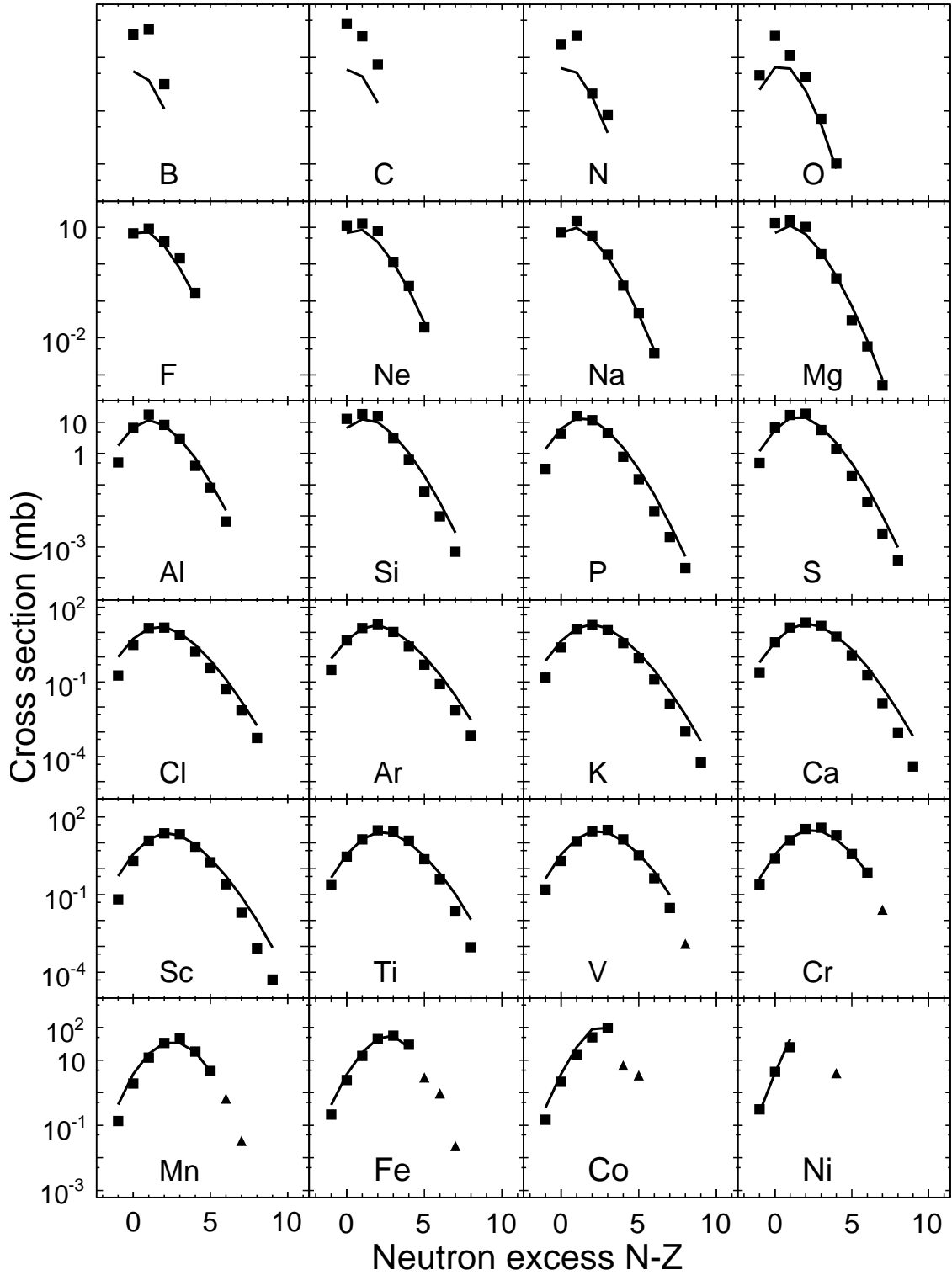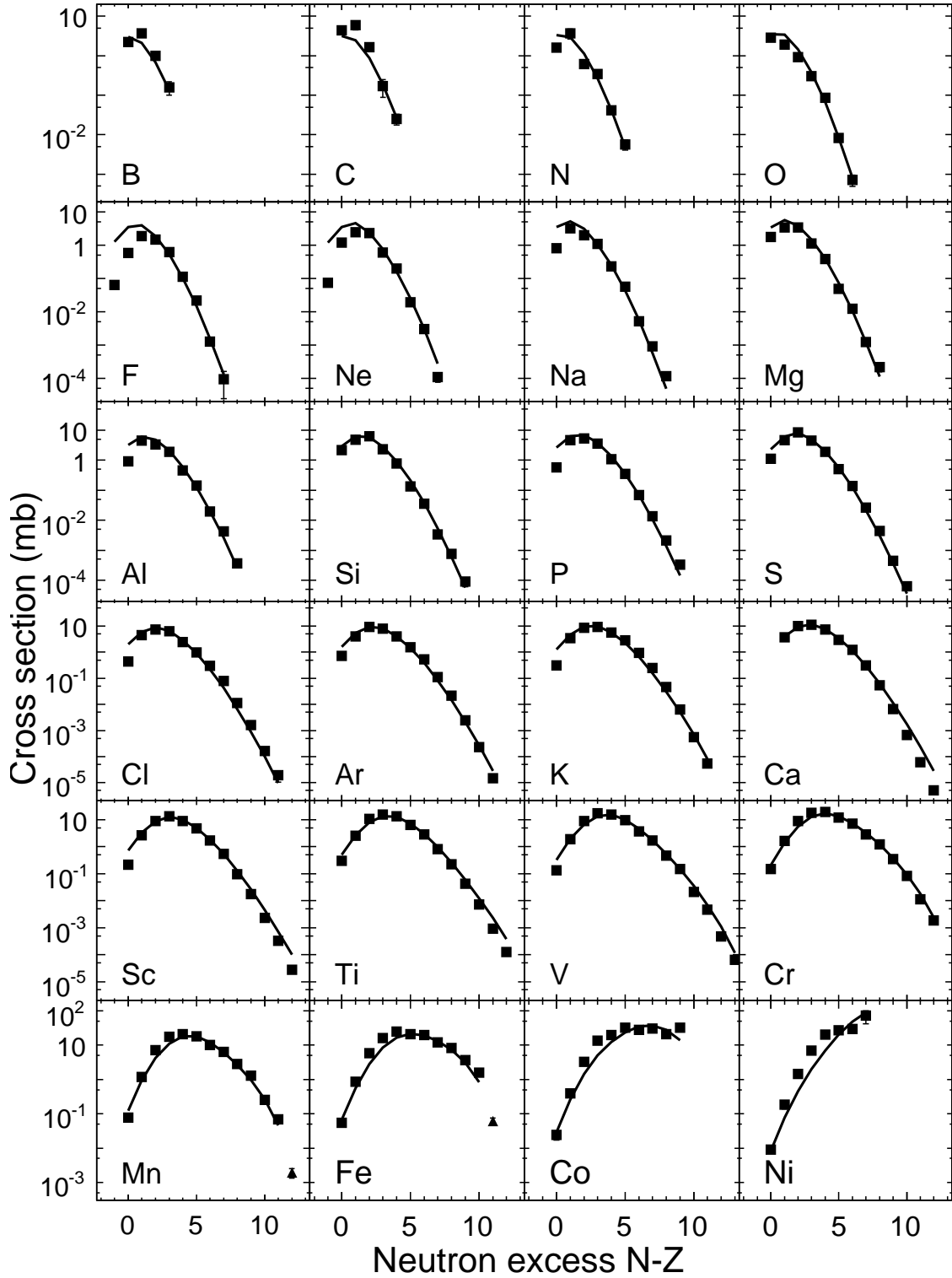
FIG. 11: Measured cross-sections presented as isotope distributions for $5 \leq Z \leq 28$ elements detected in ^{58}Ni+^{181}Ta reactions at 140 MeV/u. Experimental fragmentation data are shown as filled squares. Filled triangles show the cross-sections of nucleon pick-up reactions. EPAX predictions are shown as solid lines.

FIG. 12: Measured cross-sections presented as isotope distributions for $5 \leq Z \leq 28$ elements detected in ^{64}Ni+^{9}Be reactions at 140 MeV/u. Experimental fragmentation data are shown as filled squares. Filled triangles show the cross-sections of nucleon pick-up reactions. EPAX predictions are shown as solid lines.
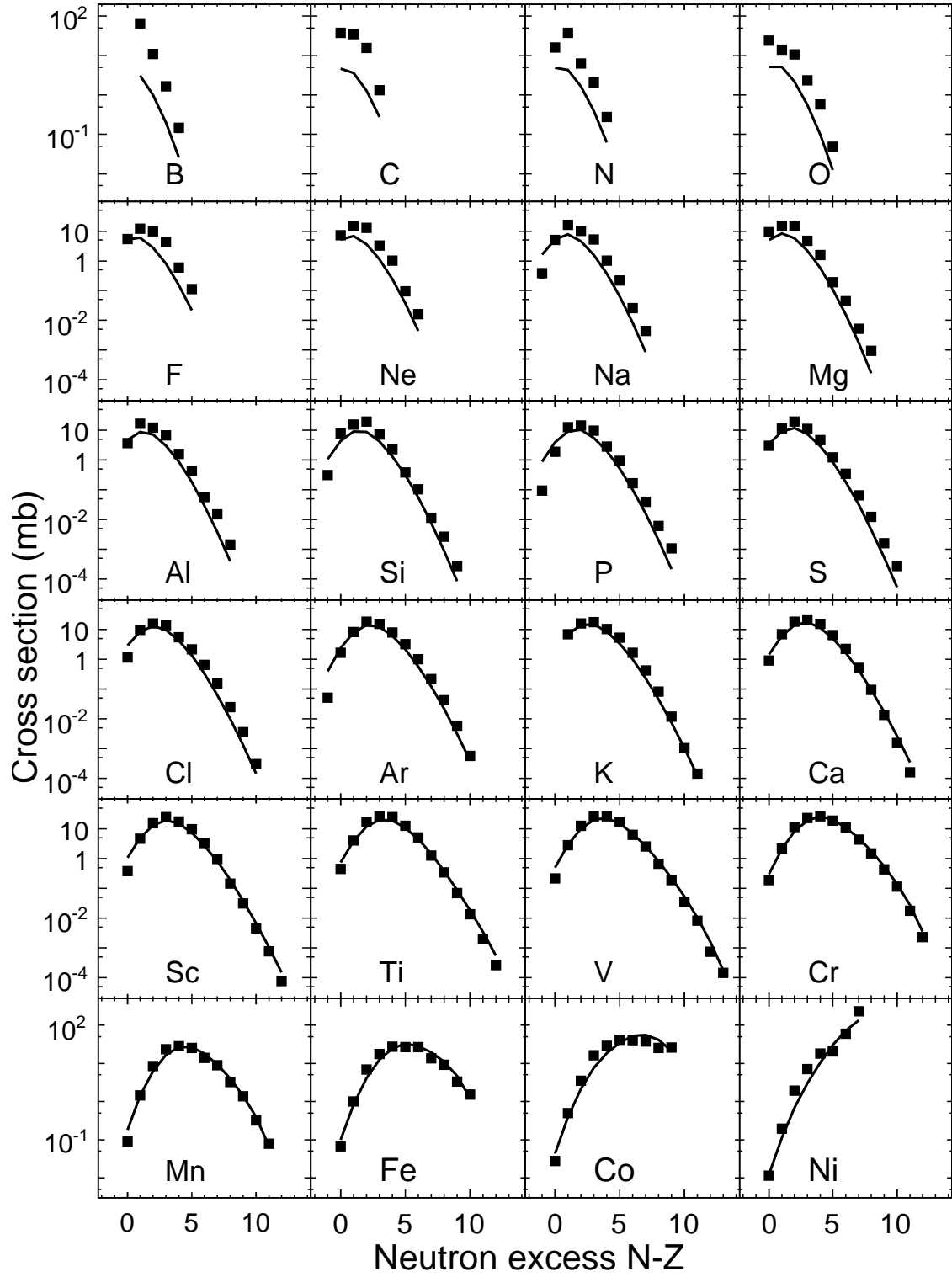
FIG. 13: Measured cross-sections presented as isotope distributions for $5 \leq Z \leq 28$ elements detected in ^{64}Ni+^{181}Ta reactions at 140 MeV/u. Experimental fragmentation data are shown as filled squares. EPAX predictions are shown as solid lines.
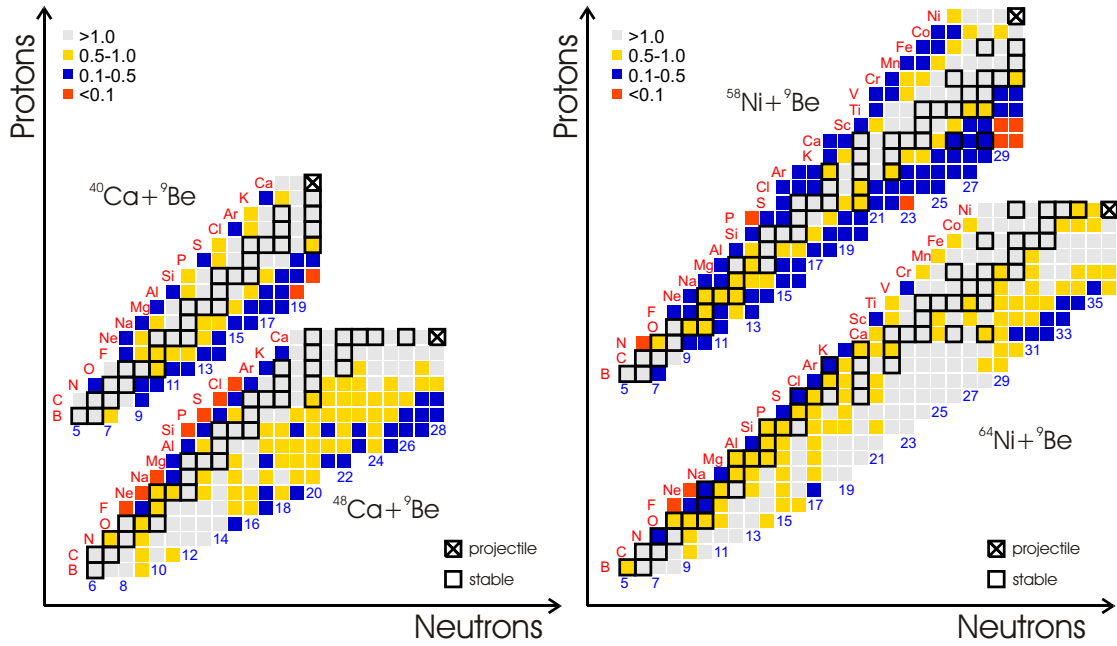
FIG. 14: (Color online) Ratios of measured fragment cross sections and predicted cross-sections from EPAX parameterization for ^{40,48}Ca projectiles on ^{9}Be target (left panel) and ^{58,64}Ni projectiles on ^{9}Be target (right panel). The lightest grey color represents ratios with values greater than 1.